Scanning Microscopy Vol. 11, 1997 (Pages 277-286) 0891-7035/97$5.00+.25
Scanning Microscopy International, Chicago (AMF O'Hare), IL 60666 USA

SIMULATION OF TRANSMISSION AND SCANNING TRANSMISSION ELECTRON MICROSCOPIC IMAGES CONSIDERING ELASTIC AND THERMAL DIFFUSE SCATTERING

C. Dinges and H. Rose*

Institute of Applied Physics, Darmstadt University of Technology, Darmstadt, Germany

Abstract

A reliable image simulation procedure for transmission (TEM) and scanning transmission (STEM) electron microscopic images must take into account plural elastic scattering, inelastic scattering and thermal diffuse scattering. The intensity of the simulated images depends strongly on the elastic scattering amplitude and the models chosen to describe inelastic and thermal diffuse scattering. Our improved image simulation procedure utilizes the approximation proposed by Weickenmeier and Kohl for the elastic scattering amplitude instead of the Doyle-Turner approximation. Thermal diffuse scattering is treated in terms of the Einstein model. In this paper, simulated TEM diffraction patterns and high-angle annular dark-field (HAADF) STEM images of thick crystals of silicon are used to demonstrate the influence of plural elastic and thermal diffuse scattering on the image formation. The comparison of calculated TEM diffraction patterns using the two different approximations for the elastic scattering amplitude shows that the use of the Doyle-Turner approximation results in a smaller image intensity in the range of large scattering angles. Simulated HAADF STEM images for different thicknesses of a silicon crystal show strong influence of the dynamical calculation on image formation for thick specimens. In this case a theory fails which describes the image formation process by a simple convolution of a probe function with an object function.

Key Words: Image simulation, high-angle annular dark-field scanning transmission electron microscopic images, transmission electron microscopy diffraction patterns, plural elastic scattering, thermal diffuse scattering, elastic scattering amplitude, Einstein model, frozen lattice approximation.

*Address for correspondence:
H. Rose
Institute of Applied Physics, TU Darmstadt
Hochschulstrasse 6, 64289 Darmstadt, Germany
Telephone number: +49 6151 162718
FAX number: +49 6151 166053
E-mail: rose@ltoi.iap.physik.tu-darmstadt.de

Introduction

In the past, several attempts have been made to include thermal diffuse scattering and inelastic scattering into the theory of image formation in electron microscopy. The approaches of Rose (1984), Wang (1995) and Dinges *et al.* (1995) are based on the multislice formalism (Cowley and Moodie, 1957) which allows the calculation of inelastically filtered images for transmission (TEM) and scanning transmission (STEM) electron microscopy. Allen and Roussow (1993) proposed an ansatz using the Bloch wave formalism.

Thermal diffuse scattering has been included into an image simulation procedure for the first time by Xu *et al.* (1990). The authors introduced the so-called frozen lattice model. This model is based on the approximation that the time for the electron to pass through the object is much smaller than the vibration period of the atoms. Therefore, each electron interacts with another configuration of the atoms. To obtain the resulting intensities one must add up the image intensity of all partial images resulting from the different configurations of the atoms. The calculation of such an image is very simple: one performs several multislice calculations for different configurations of the atoms and sums up the resulting images incoherently. The individual lattice configurations can be obtained by assuming simple models for the atomic vibrations, e.g., the Einstein model.

In our previous paper (Dinges *et al.*, 1995) we have described another possibility for the calculation of images which considers plural elastic scattering, inelastic scattering and thermal diffuse scattering. We have shown that the averaging over the different configurations of atoms can be performed semi-analytically if the Einstein model is applied. This model assumes that each atom oscillates independently along the three coordinate axes. Our calculations result in transmission functions which can be used for the multislice formalism.

In the following, we refer to our image simulation program (Dinges *et al.*, 1995). In the second (theoretical) section it will be shown that the use of the Weickenmeier-Kohl approximation (Weickenmeier and Kohl, 1991) for the elastic scattering amplitude allows the calculation of analytical expressions which describe thermal diffuse

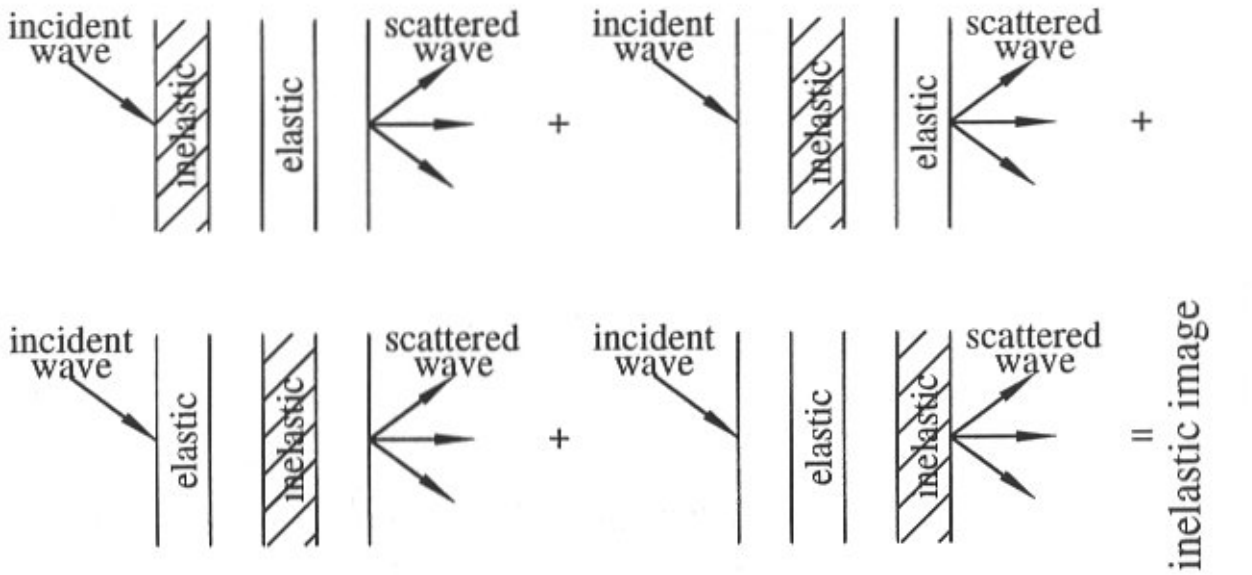

Figure 1. Simulation of images considering single thermal diffuse scattering and plural elastic scattering. Elastic scattering events occur in the blank slices. Thermal diffuse scattering events occur in the hatched slices. A detailed descriction is given in the section on "Modified Multislice Formalism".

scattering. In the third section the working scheme of our image simulation procedure is explained using a simple example. In the forth section the new analytical expressions are applied to the image simulation. First, a simulated TEM diffraction pattern of a 50 nm thick crystal of silicon is compared with a previously published image (Dinges and Rose, 1996). Then the influence of thermal diffuse scattering on HAADF STEM images is discussed. The results of our image simulation procedure are compared with those obtained by Hillyard and Silcox (1995) using the frozen lattice approximation and the Einstein model. In addition the influence of crystal thickness on the image intensity in HAAD STEM images is discussed in detail. The main results of the paper are summarized in the fifth section.

Theory Based on Improved Scattering Amplitudes

In our previous work (Dinges *et al*., 1995; Dinges and Rose, 1996) we employed the Doyle-Turner approximation for the electron scattering amplitude. In this case the scattering amplitude is given as the sum of four Gauss functions:

$$f(\vec{K}) = \sum_{i=1}^{4} A_i \exp\{-B_i K^2\} \qquad (1)$$

where K denotes the scattering vector and A_i and B_i are constants tabled by Doyle and Turner (1968) and Smith and Burge (1962). Unfortunately, this fit is only valid in the range of scattering vectors up to $K < 4\pi \cdot 2\text{Å}^{-1}$. The calculation of diffraction patterns of thick crystalline specimens which employs this approximation underestimates high-angle scattering and, therefore, leads to erroneous intensities for the diffraction spots (Fox *et al*., 1989; Bird and King 1990; Weickenmeier and Kohl, 1991).

This approximation has also been used to obtain analytical expressions for phonon scattering. In this case the correct structure of the phonon background in the diffraction patterns is obtained because this structure is largely determined by the symmetry of the crystalline specimen. Nevertheless, the absolute intensity of the phonon background is still underestimated.

In the past several routines have been developed (Fox *et al*., 1989; Bird and King, 1990; Weickenmeier and Kohl, 1991) which approximate the elastic scattering amplitude in the full range up to $K < 4\pi \cdot 6\text{Å}^{-1}$ tabled by Doyle and Turner (1968). Here we will show that the improved approximation for the elastic scattering amplitude

$$f(\vec{K}) = \frac{1}{K^2} \sum_{v=1}^{5} \tilde{A}_v (1 - \exp\{-\tilde{B}_v K^2\}) \qquad (2)$$

given by Weickenmeier and Kohl (1991) yields analytical expressions for the phonon transmission functions.

An appropriate starting point for the calculation of the improved transmission function of a thin slice is the mutual dynamic object transparency (MDOT) $M(\vec{\rho},\vec{\rho}')$ which can be written (Dinges *et al*., 1995) as

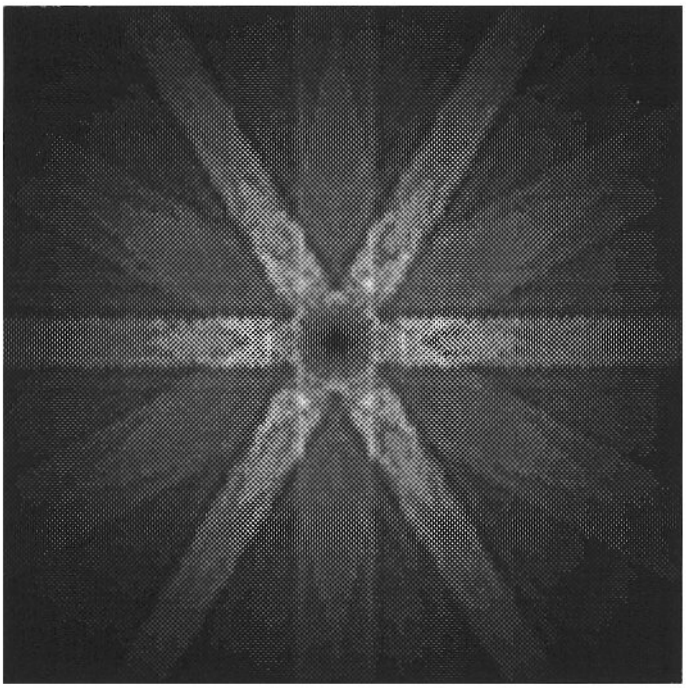

Figure 2. Calculated background diffraction pattern of Si in <111>-orientation caused by thermal diffuse scattering employing the improved Weickenmeier-Kohl approximation for the scattering amplitude.

$$M(\vec{\rho},\vec{\rho}') = \exp\{i(<\chi>-<\chi'>) - \frac{1}{2}(\mu_2^{(ph)}(\vec{\rho}) + \mu_2^{(ph)}(\vec{\rho}')) + \mu_{11}^{(ph)}(\vec{\rho},\vec{\rho}')\} \tag{3}$$

$$\approx \exp\{i(<\chi>-<\chi'>) - \frac{1}{2}(\mu_2^{(ph)}(\vec{\rho}) + \mu_2^{(ph)}(\vec{\rho}'))\} + \mu_{11}^{(ph)}(\vec{\rho},\vec{\rho}')\exp\{i(<\chi>-<\chi'>)\}$$

$$= T^{(ab)}(\vec{\rho})T^{(ab)*}(\vec{\rho}') + \mu_{11}^{(ph)}(\vec{\rho},\vec{\rho}')T(\vec{\rho})T^{*}(\vec{\rho}') \tag{4}$$

The transmission functions T and $T^{(ab)}$ are defined as

$$T(\vec{\rho}) = \exp\{i<\chi(\vec{\rho})>\} \tag{5}$$

$$T^{(ab)}(\vec{\rho}) = \exp\{-\frac{1}{2}\mu_2(\vec{\rho})\}T(\vec{\rho}) \tag{6}$$

where

$$<\chi> = \sum_i <\chi_i>$$

$$= \sum_i \frac{1}{2\pi k}\int f_i(\vec{K})\exp\{-u_i^2K^2/4\}\exp\{-i\vec{K}(\vec{\rho}-\vec{\rho}_i 0)\}d^2\vec{K} \tag{7}$$

is the thermally averaged phase shift,

$$\mu_{11}^{(ph)} = (\frac{1}{2\pi k})^2 \sum_i \int\int f_i(\vec{K})f_i(\vec{K}')\exp\{-u_i^2(\vec{K}-\vec{K}')^2/4\} \times \exp\{-i\vec{K}(\vec{\rho}-\vec{\rho}_i 0)\}\exp\{i\vec{K}'(\vec{\rho}'-\vec{\rho}_i 0)\}d^2\vec{K}d^2\vec{K}'$$

$$-(\frac{1}{2\pi k})^2 \sum_i \int\int f_i(\vec{K})f_i(\vec{K}')\exp\{-u_i^2(K^2+K'^2)/4\} \times \exp\{-i\vec{K}(\vec{\rho}-\vec{\rho}_i 0)\}\exp\{i\vec{K}'(\vec{\rho}'-\vec{\rho}_i 0)\}d^2\vec{K}d^2\vec{K}' \tag{8}$$

the phonon term and

$$\mu_2^{(ph)}(\vec{\rho}) = \mu_{11}^{(ph)}(\vec{\rho},\vec{\rho}) \tag{9}$$

the absorption potential. The mean square vibration amplitude of the i-th atom is denoted by u_i^2. The transmission function $T^{(ab)}(\vec{\rho})$ considers the effect of phonon scattering only by means of an absorption potential. This incomplete approximation merely results in a damping of the image intensity. By employing this transmission function for the simulation of TEM diffraction patterns, one only obtains a slight change in the intensities of the diffraction spots, yet never a diffuse background. To obtain the diffuse background the term $\mu_{11}^{(ph)}(\vec{\rho},\vec{\rho}')\,T(\vec{\rho})T^{*}(\vec{\rho}')$ must be incorporated in the image simulation. It has been shown previously (Dinges *et al.*, 1995) that an appropriate factorization of $\mu_{11}^{(ph)}(\vec{\rho},\vec{\rho}')$ is possible. In this case the well-known multislice formalism (Cowley and Moodie, 1957) can be applied for the image simulation. The factorization can

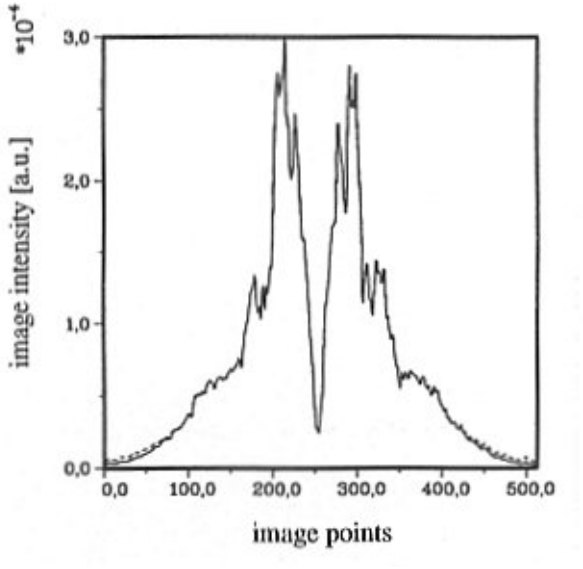

Figure 3. Linescans across the two diffraction patterns shown in Figure 2; the curve (---) corresponds to Figure 2a, the curve (- - -) to Figure 2b.

---

be written as a sum of products. Each product consists of two factors, one is a function of $\vec{\rho}$, the other a function of $\vec{\rho}'$. Reducing the sum of products to a sum of factors multiplied by an additional random phase factor leads to the phonon transmission function. Multiplying this function with its conjugate complex and averaging over the random phase factors results in the MDOT for a thin slice.

Rewriting the elastic scattering amplitude (Weickenmeier and Kohl, 1991) as

$$f(\vec{K}) = \frac{1}{K^2}\sum_{\nu=1}^{5}\tilde{A}_\nu\left(1-\exp\{-\tilde{B}_\nu K^2\}\right) = \sum_{\nu=1}^{5}\tilde{A}_\nu\int_0^{\tilde{B}_\nu}\exp\{-B_\nu K^2\}\,dB_\nu \tag{10}$$

shows that this approximation can be expressed as a sum of integrals over exponential functions with K^2 as parameter. Therefore, the formulae given in our first paper (Dinges *et al*., 1995) can be applied, where the constants A_i must be replaced by $\tilde{A}_i$ and the additional integrations over B_i must be performed in all corresponding formulae.

Performing this integration for $\langle\chi\rangle$ results in

$$\begin{aligned}
\langle\chi_i\rangle &= \frac{1}{2k}\sum_\nu\int_0^{\tilde{B}_\nu}\frac{\tilde{A}_\nu}{B_\nu+u_i^2/4}\exp\{-\frac{(\vec{\rho}-\vec{\rho}_{i0})^2}{4B_\nu+u_i^2}\}\,dB_\nu \\
&= \frac{1}{2k}\sum_\nu\tilde{A}_\nu\int_{(\vec{\rho}-\vec{\rho}_{i0})^2/(4\tilde{B}_\nu+u_i^2)}^{(\vec{\rho}-\vec{\rho}_{i0})^2/u_i^2}\frac{\exp\{-y\}}{y}\,dy \\
&= \frac{1}{2k}\sum_\nu\tilde{A}_\nu\left[E_1\left(\frac{(\vec{\rho}-\vec{\rho}_{i0})^2}{4\tilde{B}_\nu+u_i^2}\right)-E_1\left(\frac{(\vec{\rho}-\vec{\rho}_{i0})^2}{u_i^2}\right)\right]
\end{aligned} \tag{11}$$

The function $E_1(x)$ in the last expression denotes the integral logarithm

$$E_1(x) = \int_x^\infty\frac{\exp\{-y\}}{y}dy \tag{12}$$

The somewhat lengthy calculation of the phonon transmission function leads to

$$\begin{aligned}
&T^{(ph1)}(\vec{\rho},\vec{\alpha}) \\
&= \exp\{i\langle\chi\rangle\}\sum_i\frac{1}{2k}\sum_\mu\frac{\tilde{A}_\mu}{\rho^2}\Big\{\Big\{\exp\Big[-\frac{(\vec{\rho}-\vec{\rho}_{i0})^2}{4\tilde{B}_\mu+u_i^2}\Big] \\
&\quad-\exp\Big[-\frac{(\vec{\rho}-\vec{\rho}_{i0})^2}{u_i^2}\Big]\Big\}\times\sqrt{2}\,u_i(\vec{\rho}-\vec{\rho}_{i0})\begin{pmatrix}e^{i\alpha_{1i}}\\ e^{i\alpha_{2i}}\end{pmatrix} \\
&\quad+\frac{u_i^2}{\sqrt{2}}\Big\{\exp\Big[-\frac{(\vec{\rho}-\vec{\rho}_{i0})^2}{4\tilde{B}_\mu+u_i^2}\Big]\Big(3+2\frac{(\vec{\rho}-\vec{\rho}_{i0})^2}{4\tilde{B}_\mu+u_i^2}\Big) \\
&\quad-\exp\Big[-\frac{(\vec{\rho}-\vec{\rho}_{i0})^2}{u_i^2}\Big]\Big(3+2\frac{(\vec{\rho}-\vec{\rho}_{i0})^2}{u_i^2}\Big)\Big\}e^{i\alpha_{3i}}
\end{aligned} \tag{13}$$

and

$$\begin{aligned}
T^{(ph2)}(\vec{\rho},\vec{\alpha}) &= \exp\{i\langle\chi\rangle\}\sum_i\frac{1}{2k}\sum_\mu\frac{\sqrt{3}}{\sqrt{2}}\frac{\tilde{A}_\mu}{\rho^2}u_i^2 \\
&\times\Big[\exp\Big\{-\frac{(\vec{\rho}-\vec{\rho}_{i0})^2}{4\tilde{B}_\mu+u_i^2}\Big\}-\exp\Big\{-\frac{(\vec{\rho}-\vec{\rho}_{i0})^2}{u_i^2}\Big\}\Big]e^{i\alpha_{4i}}
\end{aligned} \tag{14}$$

The details of the calculation and the absorption potential $\mu_2^{(ph)}(\vec{\rho})$ are given in Appendix A. We obtain two transmission functions because the last term in Equation (24) (Appendix A) contains a negative sign. To determine the image including phonon scattered electrons, the improved multislice formalism must be used three times: First, one has to calculate the image by considering plural elastic scattering and phonon scattering by means of the

absorption potential. In the next step a partial image is calculated using the phonon transmission function $T^{(ph1)}$. The third step determines the "negative" partial image by means of the second phonon transmission function $T^{(ph2)}$. This image must be subtracted from the other two images because of the negative sign in Equation (24).

Modified Multislice Formalism

In the following discussion we restrict ourself to plural elastic scattering and thermal diffuse scattering. Inelastic scattering is not taken into account. Nevertheless, for a complete description of the image formation process inelastic scattering should not be neglected.

In the previous section thermal diffuse scattering has been considered by applying the Einstein model. This model describes each atom as an independent oscillator along the three coordinate axes. Therefore, scattered electron waves originating from thermal diffuse scattering processes at different atoms must be superimposed incoherently. In contrast scattered electron waves resulting from elastic scattering must be superimposed coherently. In the previous section we have calculated transmission functions which describe elastic scattering and thermal diffuse scattering. These transmission functions are applied to simulate images. The calculation has shown that it is necessary to divide the simulation process into two steps:

In the first step an image calculation is performed which takes into account plural elastic scattering and thermal diffuse scattering by means of an absorption potential. The absorption potential describes the influence of an (imaginary) energy filter which removes the thermal diffuse scattered electrons from the electron beam. Therefore, the resulting image intensity is damped in comparison to the intensity of an image which has been calculated considering only plural elastic scattering. This image is obtained by performing a well-known multislice calculation.

In the second step an image is calculated with the modified multislice formalism. Every electron wave which contributes to this image has performed at least one thermal diffuse scattering process. In this case an energy filter eliminates all purely elastically scattered electrons from the beam. As mentioned above the scattered waves stemming from thermal diffuse scattering processes at different atoms must be superimposed incoherently. Figure 3 shows the working scheme for the calculation of the "inelastic" image. In this example we consider an object divided in four slices. There should be no empty slice. For a proper calculation taking into account plural elastic scattering and single thermal diffuse scattering one has to perform several multislice calculations. Thermal diffuse scattering occurs with equal probability in one of the four slices, because the mean free path length is large compared to the entire thickness of the object. If each slice contains only one atom the calculation of the second step image is finished after performing the four cases for scattering events depicted in Figure 3. Normally, there are several atoms in each slice. In this case the scattered waves stemming from thermal diffuse scattering processes at different atoms must be superimposed incoherently. To ensure this incoherent superposition of the inelastically scattered waves emanating from the atoms of the first slice, a multislice formalism must be performed for each atom in the first slice using the phonon transmission function for this slice and the elastic transmission function for the other three slices. Subsequently the images intensities obtained from each of these calculations must be superimposed. The same procedure occurs for thermal diffuse scattering in the other three slices. Therefore, one has to perform $\Sigma_n i_n$ multislice calculations to obtain the image. The index n denotes the slice, in which thermal diffuse scattering occurs, the symbol i indicates the number of atoms in this slice.

Since one deals with thick objects consisting of a large number of atoms in a unit cell, one can use a trick to reduce the calculation time. By introducing statistical phases it is possible to calculate images considering thermal diffuse scattering and plural elastic scattering rather fast. Assuming that thermal diffuse scattering occurs in the first slice one has to multiply the corresponding scattered waves with random phase factors. After performing a few number of multislice calculations with different sets of statistical phases, the interference terms between waves emanating from different atoms cancel out in the averaged image.

The frozen lattice model can also be applied for our model. In this case one has to perform the multislice calculations by using different configurations of the atoms in each of the four slices where thermal diffuse scattering occurs. Therefore the calculation time is comparable for the two models.

Image Simulation

In the following simulated TEM diffraction patterns are used to demonstrate the differences in the image intensity resulting from the chosen approximation for the elastic scattering amplitude.

To investigate the influence of phonon scattering on HAADF STEM images of thick crystalline objects, linescans through such images for a 20 nm thick crystal of silicon in <110>-orientation have been calculated. By employing the imaging conditions chosen by Hillyard and Silcox (1995), we can compare the results of our simulation with their results which are based on the frozen phonon approximation.

By varying the specimen thickness for distinct probe positions, we can roughly determine the fraction of image

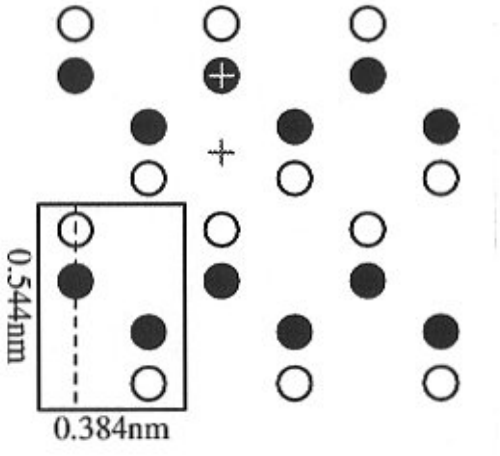

Figure 4. Si in <ll0>-orientation. The atoms located in the plane $c = 0.192$ nm are drawn black, the atoms marked white are positioned in the plane $c = 0$ nm. The dashed line marks the linescans depicted in Figure 5. The two crosses indicate the probe positions for the thickness series presented in Figure 6.

intensity which stems from thermal diffuse scattering as a function of thickness.

Simulation of TEM diffraction patterns

Simulated TEM diffraction patterns of a simple crystalline object are well suited for demonstrating the differences in image intensity which result from the use of different approximations for the scattering amplitude. The calculations have been performed for a 50nm thick crystal of silicon in <111>-orientation and a 100kV TEM. A 9 x 9 supercell of Si <111> with $a = 1.99$ nm, $b = 1.99$ nm, $c = 0.939$ nm, $\alpha = \beta = \pi/2$ and $\gamma = \pi/3$ has been assumed. The multislice calculations have been performed on a 512 x 512 matrix choosing a slice thickness $c/3$ for purely elastic scattering. For slices with single thermally diffuse scattering the thickness c was chosen. The diffraction patterns presented in Figure 2 have been obtained after averaging over ten different sets of statistical phases.

Figure 2 shows the background caused by thermal diffuse scattering taking into account only single thermal diffuse scattering and plural elastic scattering. Figure 2a has been obtained by applying the Doyle-Turner Gaussian fit for the elastic scattering amplitude, while Figure 2b represents the image calculated with the scattering amplitude given by Weickenmeier and Kohl (1991). The two images, when displayed with the same gray scales, do not differ significantly from each other. But nevertheless, there are differences, as shown in Figure 3. By taking linescans from the top left edge to the bottom right edge, the differences become clearly visible. Especially for large scattering angles the use of the Doyle-Turner Gaussian fit results in small image intensities, while those obtained by the Weickenmeier-Kohl approximation are significantly larger. This effect can be explained by the different asymptotic behaviour of the two approximations. The result for the Doyle-Turner fit decreases faster for large scattering angles than that for the approximation of Weickenmeier and Kohl which yields the correct asymptotic behaviour.

Simulation of HAADF STEM images

Hillyard and Silcox (1995) assumed a 100 kV STEM with $C_s = 0.05$ mm, $\Delta f = 13.6$ nm and an aperture angle $\theta_0 = 23$ mrad. These parameters yield a probe size of approximately 0.1 nm. Therefore, the atoms of the dumbbells in the <110>-projection of silicon (Fig. 4) are resolved. For our calculations we assume a 8 x 6 supercell with $a = 3.072$ nm, $b = 3.264$ nm and $c = 0.384$ nm. This cell is sampled on a 512 x 512 matrix. According to the distance between the two planes in which the atoms in the supercell are lying, a minimum slice thickness of 0.192 nm has been chosen for the multislice calculations. All images have been calculated by choosing a slice thickness of 4 x 0.192 nm for the slices in which thermal diffuse scattering occurs. A thickness of 0.192 nm has been chosen for slices which contain solely elastic scattering events.

An annular detector with limiting angles $\theta_{out} = 4\theta_{in}$, $\theta_{in} = 50$ mrad has been assumed. Thermal diffuse scattering is considered by using the Einstein model with a mean vibration amplitude $u_{Si} = 7.6$ pm.

Figure 5a shows linescans taken from images of a 19.2 nm thick crystal which are obtained by considering only elastic scattering (——), incorporating the effect of thermal diffuse scattering by means of an absorption potential (····) and assuming plural elastic scattering plus single thermal diffuse scattering (----). The calculations have shown that the average taken over three different sets of statistical phases leads already to reliable results. The use of more sets of statistical phases require larger computation times yet changes the calculated intensities by no more than 3%.

Figure 5b shows the scaled image intensities obtained by considering only plural elastic scattering (----) and by taking into account, in addition, thermal diffuse scattering (——).

The scaling factor has been chosen as the ratio between the mean image intensities of the two images. The comparison reveals that for the given position of the probe and detector geometry the image intensity decreases if thermal diffuse scattering is considered. This result is in good agreement with the result obtained by Hillyard and Silcox (1995). Their calculations are based on the frozen phonon approximation. The comparison between the absolute values of the intensity plots of Figure 10d in the paper of Hillyard and Silcox (1995) with those of Figure 5b leads to an additional scaling factor.

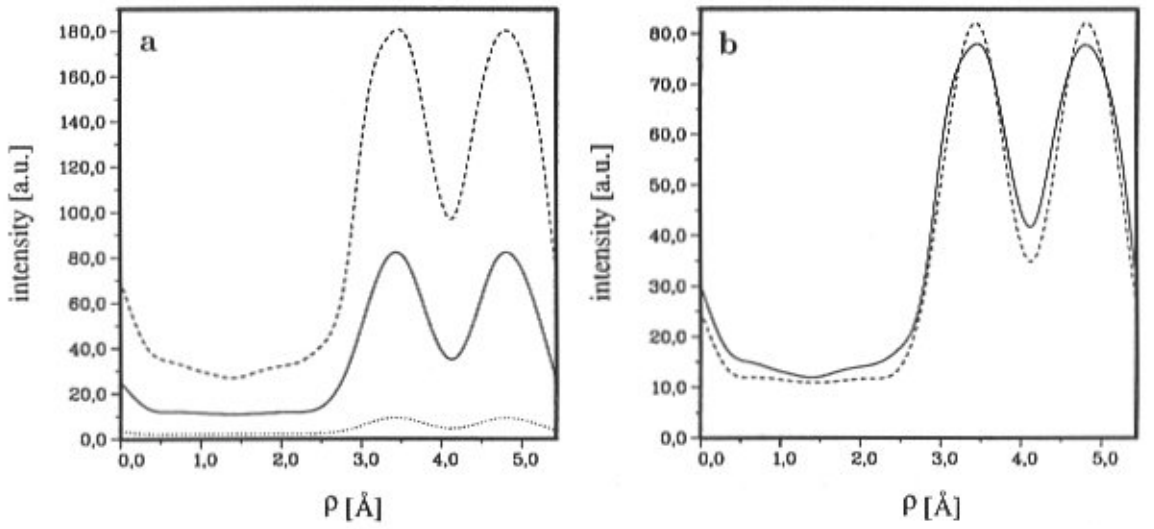

Figure 5. Linescans through HAADF STEM images of a 19.2 nm thick crystal of silicon in <110>-orientation. (**a**) unscaled image intensities obtained by considering only plural elastic scattering (____), thermal diffuse scattering by means of an absorption potential (····) and single thermal diffuse scattering and plural elastic scattering (----), (**b**) scaled image intensities obtained by considering only plural elastic scattering (----) and single thermal diffuse scattering plus plural elastic scattering (____).

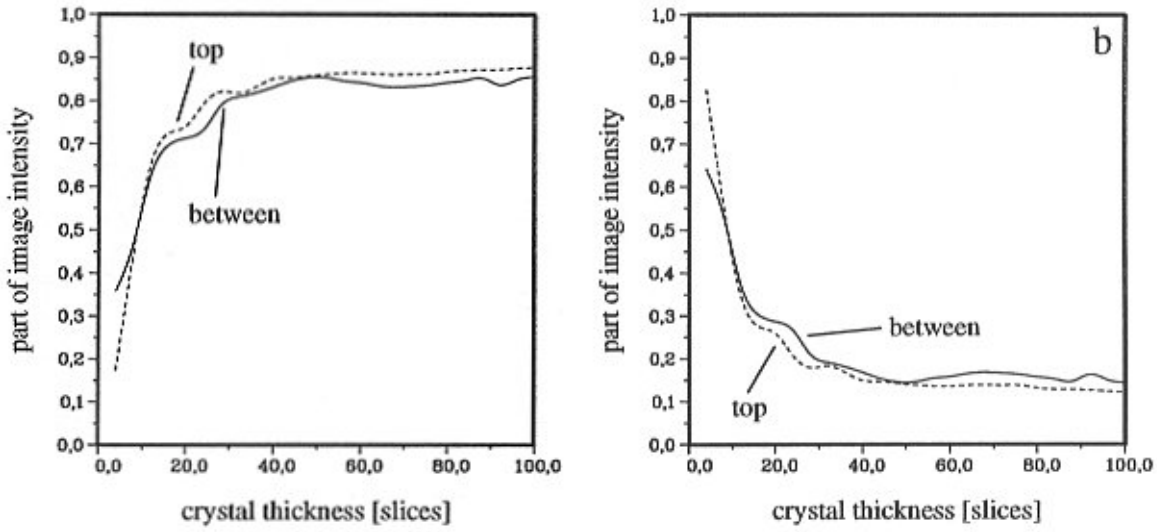

Figure 6. (**a**) Relative fraction of image intensity resulting from single thermal diffuse scattering and (**b**) from plural elastic scattering for the case where the probe is centered on the atom column (----) and where it is located midway between two adjacent columns (____). Each slice has a thickness of 0.192 nm.

Calculations based on the frozen phonon approximation are not restricted to single thermal diffuse scattering. In contrast our calculations are based on the assumption of single thermal diffuse scattering. Since the two methods produce identical results, the assumption of only single thermal diffuse scattering processes is justified for most object thicknesses used in practice.

The fact that we need two partial images to obtain the total HAADF STEM image allows us to estimate the fraction of the image intensity which stems from thermal diffuse scattering. Figure 6 shows calculated thickness series for the two positions marked in Figure 4. The calculations have been performed for the imaging conditions described above. The figure clearly demonstrates that the fraction of the image intensity that results from plural elastic scattering rapidly decreases with increasing thickness,

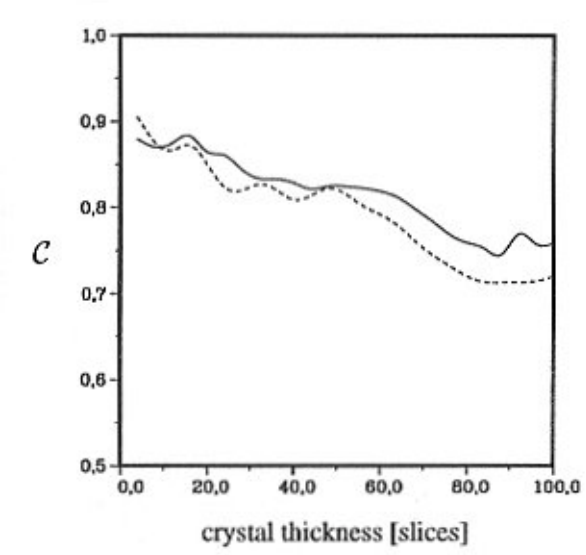

Figure 7. Column contrast *C* as a function of specimen thickness. The solid curve has been calculated by considering correctly single thermal diffuse scattering plus plural elastic scattering. The dashed curve has been obtained from images which have been calculated assuming plural elastic scattering and considering thermal diffuse scattering only by means of an absorption potential. Each slice has a thickness of 0.192 nm.

---

while the corresponding fraction of image intensity caused by thermal diffuse scattering shows the opposite behaviour. At a crystal thickness of 19.2 nm only 10% of the image intensity results from purely elastic scattering. The curves for the two different probe positions do not differ significantly from each other.

The curves depicted in Figure 6 can also be used to evaluate the column contrast as a function of specimen thickness. The column contrast is defined as

$$C = \frac{I_{top} - I_{between}}{I_{top} + I_{between}} \qquad (15)$$

where I_{top} denotes the intensity when the probe is centered on top of an atom row and $I_{between}$ is the intensity when the probe is located at the center of hexagon shown in Figure 4. The column contrast *C* resulting from Figure 6 is depicted in Figure 7. The solid curve describes the correct consideration of thermal diffuse scattering, while the dashed curve considers this effect approximately by means of an absorption potential. In both cases the contrast C decreases oscillatorily with increasing thickness. Nevertheless, even for thicker specimens the contrast is large enough to make the atom columns clearly visible in the image. For thicknesses larger than about 8 slices the column contrast *C*, obtained by including correctly the effect of thermal diffuse scattering, is always larger than that obtained by employing merely an absorption potential. The oscillations are present over the entire range of thickness. They are produced by interference effects and may serve as a measure for the "degree of coherence" of the detected signal. This "degree of coherence" strongly depends on the chosen detector geometry since it determines the fraction of the elastically scattered electrons which contributes to the signal. Experimentally the "degree of coherence" of the signal can be obtained relatively easily by means of a wedge-shaped Si crystal.

Conclusion

The use of the Doyle-Turner Gaussian fit for the elastic scattering amplitude underestimates scattering in high angles and predicts, therefore, smaller intensities in the outer regions of diffraction patterns. The implementation of the modified formulae in our program allows a more accurate simulation of filtered and unfiltered diffraction patterns.

Furthermore, we have shown that the results of our HAADF STEM image simulations which consider only single thermal diffuse scattering are in good agreement with calculations of Hillyard and Silcox (1995) who employ the frozen phonon approximation.

Our calculations of thickness series for special probe positions on a Si crystal in <ll0>-orientation demonstrate that approximately 90% of the intensity in HAADF STEM results from thermal diffuse scattering if the object thickness is larger than about 10 nm.

Acknowledgments

Financial support by the Volkswagen-Stiftung is gratefully acknowledged. We thank Dr. Earl Kirkland from Cornell University (USA) for valuable discussions. Thanks are also due to Professors J. Silcox and M. Isaacson, Cornell University, for giving one of the authors (H.R.) the opportunity to spend part of his sabbatical at the Institute of Applied and Engineering Physics.

Appendix A

The evaluation of $\mu_{11}^{(Ph)}(\vec{\rho},\vec{\rho}')_i$ by means of the Doyle-Turner approximation has been outlined (Dinges *et al*., 1995). Replacing the constants A_μ by the constants $\tilde{A}_\mu$ and adding the two integrations over B_μ and B_ν leads to $\mu_{11}^{(Ph)}(\vec{\rho},\vec{\rho}')$ in terms of the elastic scattering amplitude given by Weickenmeier and Kohl (1991):

$$\mu_{11}^{(ph)} = \left(\frac{1}{2k}\right)^2 \sum_{\mu,\nu} \int\int \{ \frac{\tilde{A}_\mu \tilde{A}_\nu}{B_\mu B_\nu + (B_\mu + B_\nu) u_i^2/4}$$

$$\times \exp\left[\frac{-4B_\nu(\vec{\rho} - \vec{\rho}_{i0})^2 - 4B_\mu(\vec{\rho}' - \vec{\rho}_{i0})^2}{16 B_\mu B_\nu + 4(B_\mu + B_\nu) u_i^2}\right]$$

$$\times \exp\left[\frac{-u_i^2[(\vec{\rho} - \vec{\rho}_{i0})^2 - (\vec{\rho}' - \vec{\rho}_{i0})]^2}{16 B_\mu B_\nu + 4(B_\mu + B_\nu) u_i^2}\right]$$

$$- \frac{A_\mu}{B_\mu + u_i^2/4} \exp\left[-\frac{(\vec{\rho} - \vec{\rho}_{i0})^2}{4(B_\mu + u_i^2/4)}\right]$$

$$\times \frac{A_\nu}{B_\nu + u_i^2/4} \exp\left[-\frac{(\vec{\rho}' - \vec{\rho}_{i0})^2}{4(B_\nu + u_i^2/4)}\right] \} d B_\mu d B_\nu \qquad (16)$$

With the abbreviations $G_\mu = B_\mu + u_i^2/4$, $G_\nu = B_\nu + u_i^2/4$ and the subsitutions $\vec{\rho} - \vec{\rho}_{i0} \rightarrow \vec{\rho}, \vec{\rho}' - \vec{\rho}_{i0} \rightarrow \vec{\rho}'$, $u_i^2/4 = x$, Equation (16) is rewritten as

$$\mu_{11}^{(ph)}(\vec{\rho}, \vec{\rho}')$$

$$= \left(\frac{1}{2k}\right)^2 \sum_{\mu,\nu} \int\int \{ \frac{\tilde{A}_\mu \tilde{A}_\nu}{G_\mu G_\nu - x^2} \exp\left[\frac{-4G_\nu \vec{\rho}^{\,2} - 4G_\mu \vec{\rho}'^2 + 8x\vec{\rho}\vec{\rho}'}{16(G_\mu G_\nu - x^2)}\right]$$

$$- \frac{\tilde{A}_\mu}{G_\mu} \exp\left[-\frac{\vec{\rho}^{\,2}}{4G_\mu} \frac{\tilde{A}_\nu}{G_\nu} \exp\left[-\frac{\vec{\rho}'^2}{4G_\nu}\right]\right] \} d B_\mu d B_\nu \qquad (17)$$

In the following only the first term of Equation 17

$$f(x) = \frac{\tilde{A}_\mu \tilde{A}_\nu}{G_\mu G_\nu - x^2} \exp\left[\frac{-4G_\nu \vec{\rho}^{\,2} - 4G_\mu \vec{\rho}'^2 + 8x\vec{\rho}\vec{\rho}'}{16(G_\mu G_\nu - x^2)}\right] \qquad (18)$$

is evaluated, because this term is not given as a sum of products, where the factors are only functions of $\vec{\rho}$ or $\vec{\rho}'$. Since x is small compared to unity, $f(x)$ can be expanded in a Taylor series

$$f(x) = \sum_{i=0}^{\infty} \frac{f^{(i)}(0)}{i!} x^i \qquad (19)$$

$$= f^{(0)}(0) + f^{(1)}(0)x + \frac{1}{2} f^{(2)}(0) x^2 + R(x) \qquad (20)$$

where $f^{(i)}(0)$ denotes the i-th derivative at $x = 0$ and $R(x)$ is the residual term.

The evaluation of the first two derivatives at $x = 0$ yields the expressions

$$f^{(0)}(0) = \frac{\tilde{A}_\mu \tilde{A}_\nu}{G_\mu G_\nu} \exp\left[\frac{-G_\nu \vec{\rho}^{\,2} - G_\mu \vec{\rho}'^2}{4G_\mu G_\nu}\right] \qquad (21)$$

$$f^{(1)}(0) = \frac{\tilde{A}_\mu \tilde{A}_\nu}{G_\mu G_\nu} \exp\left[\frac{-G_\nu \vec{\rho}^{\,2} - G_\mu \vec{\rho}'^2}{4G_\mu G_\nu}\right] \frac{\vec{\rho}\vec{\rho}'}{2G_\mu G_\nu} \qquad (22)$$

$$f^{(2)}(0) = \frac{\tilde{A}_\mu \tilde{A}_\nu}{G_\mu G_\nu} \exp\left[\frac{-G_\nu \vec{\rho}^{\,2} - G_\mu \vec{\rho}'^2}{4G_\mu G_\nu}\right]$$

$$\times \frac{(2G_\mu + \rho^2)(2G_\nu + \rho'^2) - 12G_\mu G_\nu}{4G_\mu^2 G_\nu^2} \qquad (23)$$

By inserting these relations into Equation (20) and considering $dB_\nu = dG_\nu$, we can approximately rewrite Equation (17) as follows:

$$\mu_{11}^{(ph)}(\vec{\rho}, \vec{\rho}')_i \approx \left(\frac{1}{2k}\right)^2 \sum_{\mu,\nu} \int\int \frac{\tilde{A}_\mu \tilde{A}_\nu}{G_\mu G_\nu} \exp\left[\frac{-G_\nu \vec{\rho}^{\,2} - G_\mu \vec{\rho}'^2}{4G_\mu G_\nu}\right]$$

$$\times \{ \frac{\vec{\rho}\vec{\rho}'}{2G_\mu G_\nu} x + \frac{(2G_\mu + \rho^2)(2G_\nu + \rho'^2) - 12G_\mu G_\nu}{4G_\mu^2 G_\nu^2} \frac{x^2}{2} \} d G_\mu d G_\nu \qquad (24)$$

The integration over G_ν can readily be performed. The subsequent integration over the variable G_μ yields the analytical expressions

$$\int \frac{\tilde{A}_\mu}{G_\mu} \exp\left[\frac{-\vec{\rho}^{\,2}}{4G_\mu}\right] \frac{\vec{\rho}}{\sqrt{2}\,G_\mu} \sqrt{x}\, d G_\mu$$

$$= \sqrt{8}\, A_\mu \frac{\vec{\rho} - \vec{\rho}_{i0}}{\rho^2} \frac{u_i}{2} [\exp\{-\frac{(\vec{\rho} - \vec{\rho}_{i0})^2}{4\tilde{B}_\mu + u_i^2}\} - \exp\{-\frac{(\vec{\rho} - \vec{\rho}_{i0})^2}{u_i^2}\}], \qquad (25)$$

$$\int \frac{\tilde{A}_\mu}{G_\mu} \exp\left[\frac{-\vec{\rho}^{\,2}}{4G_\mu}\right] \frac{(2G_\mu + \rho^2)}{2G_\mu^2} \frac{x}{\sqrt{2}} d G_\mu$$

$$= 4 \frac{\tilde{A}_\mu}{\rho^2} \frac{u_i^2}{4\sqrt{2}} \{ \exp\left[-\frac{(\vec{\rho} - \vec{\rho}_{i0})^2}{4\tilde{B}_\mu + u_i^2}\right] (3 + 2\frac{(\vec{\rho} - \vec{\rho}_{i0})^2}{4\tilde{B}_\mu + u_i^2})$$

$$- \exp\left[-\frac{(\vec{\rho} - \vec{\rho}_{i0})^2}{u_i^2}\right] \left(3 + 2\frac{(\vec{\rho} - \vec{\rho}_{i0})^2}{u_i^2}\right) \}, \qquad (26)$$

$$\int \frac{A_\mu}{G_\mu} \exp\left[\frac{-\vec{\rho}^{\,2}}{4G_\mu}\right] \frac{\sqrt{3}}{G_\mu} \frac{x}{\sqrt{2}}\, dG_\mu$$

$$= 4\sqrt{3}\, \frac{A_\mu}{\rho^2} \frac{u_i^2}{4\sqrt{2}} \left[\exp\left\{-\frac{(\vec{\rho}-\vec{\rho}_{i0})^2}{4\widetilde{B}_\mu + u_i^2}\right\} - \exp\left\{-\frac{(\vec{\rho}-\vec{\rho}_{i0})^2}{u_i^2}\right\}\right] \tag{27}$$

by means of which the function (24) can be expressed. The result leads to the two phonon transmission functions given in Equations (13) and (14). The necessity for two transmission functions is a consequence of the negative sign of the last term in Equation (24).

In the special case $\vec{\rho} = \vec{\rho}'$ we obtain the absorption potential $\mu_2^{(ph)}(\vec{\rho}) = \mu_{11}^{(ph)}(\vec{\rho}\vec{\rho}' = \vec{\rho})$.

By neglecting the term $f^{(2)}(0)x^2/2$, we derive the dipole approximation of phonon scattering. In this case only a single transmission function exists.

References

Allen LJ, Rossouw CJ (1993) Delocalization in electron-impact ionization in a crystalline environment. Phys Rev **B47**: 2446-2452.

Bird DM, King QA (1990) Absorptive form factors for high-energy electron diffraction. Acta Cryst **A46**: 202-*last page*.

Cowley JM, Moodie AF (1957) The scattering of electrons by atoms and crystals. I. A new theoretical approach. Acta Cryst **10**: 609-613.

Dinges C, Berger A, Rose H (1995) Simulation of TEM and STEM images considering phonon and electronic excitations. Ultramicroscopy **60**: 49-70.

Dinges C, Rose H (1996) Simulation of filtered and unfiltered TEM images and diffraction patterns. Phys stat sol (a) **150**: 23-30.

Doyle PA, Turner PS (1968) Relativistic Hartree-Fock x-ray and electron scattering factors. Acta Cryst **A24**: 390-397.

Fox AG, O'Keefe MA, Tabbernor MA (1989) Relativistic Hartree-Fock x-ray and electron atomic scattering factors at high angles. Acta Cryst **A45**: 786-793.

Hillyard S, Silcox J (1995) Detector geometry, thermal diffuse scattering and strain effects in ADF STEM imaging. Ultramicroscopy **58**: 6-17.

Rose H (1984) Information transfer in electron microscopy. Ultramircoscopy **15**: 173-192.

Smith GH, Burge RE (1962) The analytical representation of atomic scattering amplitudes for electrons. Acta Cryst **A15**: 182-*last page*.

Wang ZL (1995) *Title of chapter*. In: Elastic and Inelastic Scattering in Electron Diffraction and Imaging. Plenum, New York. Chapter 11.

Weickenmeier A, Kohl H (1991) Computation of absorptive form factors for high-energy electron diffraction. Acta Cryst **A47**: 590-603.

Xu P, Loane RF, Silcox J (1990) Energy-filtered convergent-bean electron diffraction in STEM. Ultramicroscopy **38**: 127-133.